ELSEVIER

Available online at www.sciencedirect.com

SCIENCE DIRECT®

Journal of Computational Physics 212 (2006) 778–797

JOURNAL OF COMPUTATIONAL PHYSICS

www.elsevier.com/locate/jcp

A direct multigroup-WENO solver for the 2D non-stationary Boltzmann–Poisson system for GaAs devices: GaAs-MESFET

M. Galler, F. Schürrer *

Institute of Theoretical and Computational Physics, Graz University of Technology, Petersgasse 16, A-8010 Graz, Austria

Received 15 February 2005; received in revised form 24 June 2005; accepted 5 August 2005
Available online 15 September 2005

Abstract

We propose a direct solver to the non-stationary Boltzmann–Poisson system for simulating the electron transport in two-dimensional GaAs devices. The GaAs conduction band is approximated by a two-valley model. All of the important scattering mechanisms are taken into account. Our numerical scheme consists of the combination of the multigroup approach to deal with the dependence of the electron distribution functions on the three-dimensional electron wave vectors and a high-order WENO reconstruction procedure for treating their spatial dependences. The electric field is determined self-consistently from the Poisson equation. Numerical results are presented for a GaAs-MESFET. We display electron distribution functions as well as several macroscopic quantities and compare them to those of Monte Carlo simulations. In addition, we study the influence of the used discretization on the obtained results.
© 2005 Elsevier Inc. All rights reserved.

Keywords: Boltzmann–Poisson system; Multigroup approach; WENO scheme; GaAs-MESFET; Semiconductor device simulation

1. Introduction

In this paper, we present a numerical procedure for directly solving the non-stationary Boltzmann–Poisson system for two-dimensional GaAs devices. So far, mainly stochastic methods, i.e., Monte Carlo techniques are applied for simulating the charge transport in submicron semiconductor devices [1]. However, the solution of the Boltzmann transport equations (BTEs), which govern the particle transport in semiconductors, with deterministic methods is assigned to some important advantages in comparison to Monte Carlo procedures.

* Corresponding author. Tel.: +43 316 8738177; fax: +43 316 8738677.
E-mail addresses: galler@itp.tu-graz.ac.at (M. Galler), schuerrer@itp.tu-graz.ac.at (F. Schürrer).

0021-9991/$ - see front matter © 2005 Elsevier Inc. All rights reserved.
doi:10.1016/j.jcp.2005.08.003

Standard Monte Carlo methods are unable to resolve almost empty regions of two-dimensional devices, e.g., areas close to the gate of a MESFET, while deterministic approaches can do. Hence, deterministic results should be used as benchmarks for Monte Carlo, hydrodynamic or drift-diffusion results, even though they are not competitive with Monte Carlo schemes with respect to the computation time in two dimensions. In addition, direct solution techniques to the BTEs exhibit high efficiencies in computing transient processes. They are featured by the knowledge of the particle distribution functions and not only of their moments and they give results without numerical noise even close to regions between different boundary conditions.

Thus, the direct solution of the Boltzmann transport equations has become an important alternative to the Monte Carlo simulations. As an early example, the work of Niclot et al. [2] should be mentioned. Fatemi and Odeh construced an upwind finite-difference approximation to the Boltzmann–Poisson (BP) system [3]. Majorana and Pidatella solved the BP system by means of a box method in the energy and angle variables and combined this approach with a classical discretization technique for advection equations based on upwinding in the spatial variable [4]. Carrillo et al. succeeded in introducing a deterministic high-order finite-difference WENO solver for the solution of the one-dimensional [5,6] as well as of the two-dimensional BP system for semiconductor devices [7]. In these papers, deterministic methods are presented for simulating the electron transport in silicon devices. However, schemes which allow the investigation of the carrier transport in III–V compound semiconductor devices are still rare in the literature. As very recent examples, we refer to the WENO solver for the BP system of Cáceres et al. [8] considering the electron transport in one-dimensional GaAs-diodes and to Galler and Schürrer [9] who study these devices with the help of a multigroup-WENO solver.

To close this gap for the two-dimensional case, we construct a multigroup-WENO solver for the 2D BTEs in order to determine the electron distribution functions in dependence of three momentum variables, two spatial variables and time. Therefore, we follow the main ideas proposed in [9] for simulating a 1D GaAs-diode and in [10], where a multigroup-WENO solver for 2D silicon devices is presented. We regard the multi-valley regime typical for polar semiconductors and take into account the anisotropy of some of the main scattering mechanisms of GaAs. In addition, the Poisson equation is coupled with the BTEs to describe self-consistently the electric field strength in the device.

The multigroup approach, which is applied to treat the dependence of the electron distribution function on the electron wave vector, has been used with great success for investigating the particle transport in bulk semiconductors [11–13]. It consists of a partition of the momentum space into tiny cells and the approximation of the distribution function by an appropriate ansatz, which leads to a similar approximation of the collision integral of the BTE as it was obtained in [8].

Modern semiconductors devices are featured by changes of their compositions on short length scales. Hence, suitable numerical methods for treating the spatial dependences of the distribution functions must be applied to cope, e.g., with abrupt changes in the doping concentration. Consequently, we combine our multigroup transport equations with a high-order WENO scheme [14] for approximating the spatial derivatives in the diffusion terms of the BTEs.

This paper is organized as follows. In Section 2, we summarize the basic equations which constitute the BP system for GaAs and transform them into a conservative form. The numerical scheme for solving the BP system is presented in Section 3. Finally, Section 4 deals with the application of the multigroup-WENO solver to the electron transport in a GaAs-MESFET.

2. The Boltzmann–Poisson system

We approximate the conduction band of GaAs by taking into account the Γ-valley in the center of the first Brillouin zone and four equivalent L-valleys along the crystallographic directions $\langle 1,1,1 \rangle$. The considered energy valleys are described by the non-parabolic, spherical dispersion law

$$\epsilon_v(\mathbf{k}) = \Delta_{0v} + \frac{1}{2\alpha_v}\left[\sqrt{1 + 2\alpha_v \frac{\hbar^2 k^2}{m_v^*}} - 1\right], \tag{1}$$

relating the energy ϵ_v in the valley $v = \Gamma, L$ and the electron wave vector $\mathbf{k}$ with $k = |\mathbf{k}|$ [15]. Here, Δ_{0v} denotes the gap between the minimum of the valley v and the zero energy level, which is set to the energy of the bottom of the Γ-valley. The symbols m_v^* and α_v refer to the effective mass and the non-parabolicity factor of the considered valley, respectively.

In semiconductors, the electronic states are occupied according to the electron distribution functions $f_v(t, \mathbf{x}, \mathbf{k})$, which are the probability densities to find an electron at time t at the position $\mathbf{x}$ in the valley v with the wave vector $\mathbf{k}$. The evolutions of these functions are governed by the Boltzmann transport equations [16]:

$$\frac{\partial f_v(t, \mathbf{x}, \mathbf{k})}{\partial t} + \mathbf{v}_v \cdot \nabla_{\mathbf{r}} f_v(t, \mathbf{x}, \mathbf{k}) - \frac{\mathcal{Q}}{\hbar}\mathbf{E} \cdot \nabla_{\mathbf{k}} f_v(t, \mathbf{x}, \mathbf{k}) = \mathscr{C}[f_v, f_\mu]. \tag{2}$$

Here, the group velocity is defined as $\mathbf{v}_v(\mathbf{k}) = \nabla_{\mathbf{k}}\epsilon_v(\mathbf{k})/\hbar = \hbar\mathbf{k}\{1 + 2\alpha_v[\epsilon_v(\mathbf{k}) - \Delta_{0v}]\}/m_v^*$ for $v = \Gamma, L$ in correspondence with (1). The electrostatic potential V and the related electric field strength $\mathbf{E}$ are found as the solution of the Poisson equation

$$\Delta V(t, \mathbf{x}) = -\frac{\mathcal{Q}}{\varepsilon_{\mathrm{st}}\varepsilon_0}[N_{\mathrm{D}}(\mathbf{x}) - n(t, \mathbf{x})], \quad \mathbf{E}(t, \mathbf{x}) = -\nabla V(t, \mathbf{x}), \tag{3}$$

where $\mathcal{Q}$ and $\varepsilon_{\mathrm{st}}\varepsilon_0$ label the positive elementary charge and the dielectric constant of the semiconductor, respectively. The donor density N_{D} is fixed in time, while the time-dependent electron density n is found by forming moments of the electron distribution functions:

$$n(t, \mathbf{x}) = \frac{Z_\Gamma}{4\pi^3}\int_{\mathbb{R}^3} \mathrm{d}\mathbf{k} f_\Gamma(t, \mathbf{x}, \mathbf{k}) + \frac{Z_L}{4\pi^3}\int_{\mathbb{R}^3} \mathrm{d}\mathbf{k} f_L(t, \mathbf{x}, \mathbf{k}). \tag{4}$$

The collision terms in the BTEs (2) for the scattering mechanisms ξ read in the low density approximation

$$\mathscr{C}^\xi[f_v, f_\mu] = \int_{\mathbb{R}^3} \mathrm{d}\mathbf{k}' \left[S_{\mu v}^\xi(\mathbf{k}', \mathbf{k}) f_\mu(\mathbf{k}') - S_{v\mu}^\xi(\mathbf{k}, \mathbf{k}') f_v(\mathbf{k})\right]. \tag{5}$$

In our transport model for GaAs, we regard the acoustic deformation potential scattering (ADP) and the ionized impurity scattering (IMP). The most important intravalley scattering mechanism for GaAs is the polar optical interaction (POP). Besides these intravalley scattering mechanisms, we also consider the intervalley scattering (IV) by non-polar optical phonons transferring electrons between the Γ- and L-valleys (non-equivalent intervalley scattering) and between the L-valleys (equivalent intervalley scattering). The transition rates $S_{v\mu}^\xi(\mathbf{k}, \mathbf{k}')$ of these scattering mechanisms are given in Table 1 and correspond to the expressions which are found in [17]. In this table, we use the abbreviations $\epsilon_v = \epsilon_v(\mathbf{k})$ and $\epsilon_v' = \epsilon_v(\mathbf{k}')$. In addition, $n_{\mathrm{p}} = [\exp(\hbar\omega_{\mathrm{p}}/k_{\mathrm{B}}T_{\mathrm{L}}) - 1]^{-1}$ and $n_{\mathrm{o}} = [\exp(\hbar\omega_{\mathrm{o}}/k_{\mathrm{B}}T_{\mathrm{L}}) - 1]^{-1}$ refer to the occupation number of polar and non-polar optical phonons, respectively. The overlap factor in the term of POP scattering is defined as $I_v(\mathbf{k}, \mathbf{k}') = c_v^+(\epsilon_v)c_v^+(\epsilon_v') + c_v^-(\epsilon_v)c_v^-(\epsilon_v')\mathbf{k} \cdot \mathbf{k}'/|\mathbf{k}||\mathbf{k}'|$ with $c_v^\pm(\epsilon_v) = \{[1/2 \pm 1/2 + \alpha_v(\epsilon_v - \Delta_{0v})]/[1 + 2\alpha_v(\epsilon_v - \Delta_{0v})]\}^{\frac{1}{2}}$. The screening parameter appearing in the transition rate of IMP scattering is evaluated by $q_{\mathrm{D}}^2 = \mathcal{Q}^2 N_{\mathrm{I}}/\varepsilon_{\mathrm{st}}\varepsilon_0 k_{\mathrm{B}} T_{\mathrm{L}}$. All the other symbols used in Table 1 are explained in Table 2. For more details, we refer to [16–18].

With the aim of transforming the BTE (2) in a conservative form, we introduce the following change of variables. We express the electron wave vector $\mathbf{k}_v(\epsilon, \mu, \varphi)$ in the valley v in spherical coordinates as a function of the energy ϵ, measured from the energy reference, the cosine of the polar angle μ and the azimuth angle φ:

Table 1
Transition rates $S^{\xi}_{\nu\mu}(\mathbf{k},\mathbf{k}')$ for the scattering mechanisms ξ for GaAs

ξ	$S^{\xi}_{\nu\mu}(\mathbf{k},\mathbf{k}')$
ADP	$\frac{D_A^2 k_B T_L}{4\pi^2\hbar\rho v_s^2}\delta(\epsilon'_\nu-\epsilon_\nu)$
IMP	$\frac{N_I}{\hbar}\left(\frac{\mathscr{Q}^2}{2\pi\varepsilon_{st}\varepsilon_0}\right)^2\frac{\delta(\epsilon'_\nu-\epsilon_\nu)}{(\lvert\mathbf{k}-\mathbf{k}'\rvert^2+q_D^2)^2}$
POP	$\frac{\omega_p\mathscr{Q}^2}{8\pi^2}\left(\frac{1}{\varepsilon_{hf}}-\frac{1}{\varepsilon_{st}}\right)\frac{I_\nu(\mathbf{k},\mathbf{k}')}{\lvert\mathbf{k}-\mathbf{k}'\rvert^2}[n_p\delta(\epsilon'_\nu-\epsilon_\nu-\hbar\omega_p)+(n_p+1)\delta(\epsilon'_\nu-\epsilon_\nu+\hbar\omega_p)]$
IV	$\frac{Z_\mu D_O^2}{8\pi^2\rho\omega_o}[n_o\delta(\epsilon'_\mu-\epsilon_\nu-\hbar\omega_o)+(n_o+1)\delta(\epsilon'_\mu-\epsilon_\nu+\hbar\omega_o)]$

Table 2
Material parameters for GaAs

Quantity	Symbol	Unit	Value
Mass density	ρ	kg m^{-3}	5360
Sound velocity	v_s	m s^{-1}	5240
Static dielectric constant	ε_{st}		12.90
High-frequency dielectric constant	ε_{hf}		10.92
Acoustic deformation potential	D_A	eV	7
Optical deformation potential	D_O	eV m^{-1}	10^{11}
Non-polar optical phonon energy	$\hbar\omega_o$	eV	0.032
Polar optical phonon energy	$\hbar\omega_p$	eV	0.032
Impurity concentration	N_I	cm^{-3}	10^{14}

Quantity	Symbol	Unit	Γ-valley	L-valley
Effective mass ratio	m^*_ν/m_0		0.067	0.35
Non-parabolicity factor	α_ν	e V^{-1}	0.611	0.242
Valley bottom energy	$\Delta_{0\nu}$	eV	0	0.32
Number of equivalent valleys	Z_ν		1	4

$$\mathbf{k}_\nu(\epsilon,\mu,\varphi)=k_\nu(\epsilon)(\mu,\sqrt{1-\mu^2}\cos\varphi,\sqrt{1-\mu^2}\sin\varphi), \tag{6a}$$

$$k_\nu(\epsilon)=\frac{\sqrt{2m^*_\nu}}{\hbar}\sqrt{(\epsilon-\Delta_{0\nu})[1+\alpha_\nu(\epsilon-\Delta_{0\nu})]}\Theta(\epsilon-\Delta_{0\nu}) \tag{6b}$$

with the Heaviside step-function Θ. Furthermore, we take into account that f_ν only depends on the variables t, x, y, ϵ, μ and φ for spatially two-dimensional problems with inhomogeneities in the x- and y-direction. Based on the change of variables (6a) and the features of f_ν, some algebra reveals that the BTE (2) can be transformed into

$$\frac{\partial\Phi_\nu}{\partial t}+\frac{\partial(g_1^\nu\Phi_\nu)}{\partial x}+\frac{\partial(g_2^\nu\Phi_\nu)}{\partial y}+\frac{\partial(g_3^\nu\Phi_\nu)}{\partial\epsilon}+\frac{\partial(g_4^\nu\Phi_\nu)}{\partial\mu}+\frac{\partial(g_5^\nu\Phi_\nu)}{\partial\varphi}=\mathscr{C}[\Phi_\nu,\Phi_\mu]. \tag{7}$$

This expression contains the new unknown functions

$$\Phi_\nu(t,x,y,\epsilon,\mu,\varphi)=\mathscr{D}_\nu(\epsilon)f_\nu(t,x,y,\epsilon,\mu,\varphi) \tag{8}$$

for $\nu=\Gamma, L$ with the Jacobian of the transformation (6)

$$\mathscr{D}_\nu(\epsilon)=\frac{m^*_\nu}{\hbar^3}\sqrt{2m^*_\nu(\epsilon-\Delta_{0\nu})[1+\alpha_\nu(\epsilon-\Delta_{0\nu})]}[1+2\alpha_\nu(\epsilon-\Delta_{0\nu})]\Theta(\epsilon-\Delta_{0\nu}), \tag{9}$$

which equals the density of states except for a constant factor. The rewritten collision integral reads

$$\mathscr{C}^{\xi}[\Phi_{v}, \Phi_{\mu}] = \int_{\mathscr{D}} \mathrm{d}\mathbf{S}' \left[S^{\xi}_{\mu v}(\mathbf{k}'_{\mu}, \mathbf{k}_{v}) \mathscr{D}_{v}(\epsilon) \Phi'_{\mu} - S^{\xi}_{v\mu}(\mathbf{k}_{v}, \mathbf{k}'_{\mu}) \mathscr{D}_{\mu}(\epsilon') \Phi_{v} \right] \tag{10}$$

with $\mathrm{d}\mathbf{S}' = \mathrm{d}\epsilon' \mathrm{d}\mu' \mathrm{d}\varphi'$, $\mathscr{D} = [(0,\infty) \times [-1,1] \times [0,2\pi]$, $\mathbf{k}_v = \mathbf{k}_v(\epsilon, \mu, \varphi)$, $\mathbf{k}'_\mu = \mathbf{k}_\mu(\epsilon', \mu', \varphi')$, $\Phi_v = \Phi_v(t,x,y,\epsilon,\mu,\varphi)$ and $\Phi'_\mu = \Phi_\mu(t,x,y,\epsilon',\mu',\varphi')$. In addition, the functions g^v_l, $l = 1,2,\ldots,5$ are defined as

$$g^v_1(\cdot) = \frac{\hbar}{m^*_v} \frac{k^v(\epsilon)}{1 + 2\alpha_v(\epsilon - \Delta_{0v})} \mu, \tag{11a}$$

$$g^v_2(\cdot) = \frac{\hbar}{m^*_v} \frac{k^v(\epsilon)}{1 + 2\alpha_v(\epsilon - \Delta_{0v})} \sqrt{1-\mu^2} \cos\varphi, \tag{11b}$$

$$g^v_3(\cdot) = -\frac{\mathscr{Q}}{m^*_v} \frac{k^v(\epsilon)}{1 + 2\alpha_v(\epsilon - \Delta_{0v})} \left[E_x(t,x,y)\mu + E_y(t,x,y)\sqrt{1-\mu^2}\cos\varphi \right], \tag{11c}$$

$$g^v_4(\cdot) = -\frac{\mathscr{Q}}{\hbar} \frac{\sqrt{1-\mu^2}}{k_v(\epsilon)} \left[E_x(t,x,y)\sqrt{1-\mu^2} - E_y(t,x,y)\mu\cos\varphi \right], \tag{11d}$$

$$g^v_5(\cdot) = \frac{\mathscr{Q}}{\hbar} \frac{E_y(t,x,y)}{k_v(\epsilon)\sqrt{1-\mu^2}} \sin\varphi. \tag{11e}$$

The functions g^v_3, g^v_4 and g^v_5 contain the x- and y-component of the electric field, determined from the 2D Poisson equation

$$E_x(t,x,y) = -\frac{\partial}{\partial x} V(t,x,y), \quad E_y(t,x,y) = -\frac{\partial}{\partial y} V(t,x,y), \tag{12a}$$

$$\frac{\partial^2}{\partial x^2} V(t,x,y) + \frac{\partial^2}{\partial y^2} V(t,x,y) = -\frac{\mathscr{Q}}{\varepsilon_{\mathrm{st}}\varepsilon_0} [N_{\mathrm{D}}(x,y) - n(t,x,y)]. \tag{12b}$$

3. Numerical scheme

In this section, we introduce the numerical scheme used to solve the BP system (7) and (12b). To begin with, we treat the dependences of the unknown functions Φ_v on the independent variables ϵ, μ and φ by means of the multigroup approach. Therefore, we discretize these variables according to

$$\epsilon^v_{i+\frac{1}{2}} = \Delta_{0v} + i\Delta\epsilon, \quad i = 0,1,\ldots,N_v, \ \ \Delta\epsilon = \frac{\hbar\omega_{\mathrm{p}}}{n_{\mathrm{mul}}}, \tag{13a}$$

$$\mu_{j+\frac{1}{2}} = j\Delta\mu - 1, \quad j = 0,1,\ldots,M, \ \ \Delta\mu = \frac{2}{M}, \ \ M = 2m_{\mathrm{mul}}, \tag{13b}$$

$$\varphi_{k+\frac{1}{2}} = k\Delta\varphi, \quad k = 0,1,\ldots,R, \ \ \Delta\varphi = \frac{\pi}{R}, \ \ R = 2r_{\mathrm{mul}} \tag{13c}$$

with $n_{\mathrm{mul}}, m_{\mathrm{mul}}, r_{\mathrm{mul}} \in \mathbb{N}$. In (13c), we take advantage of the mirror symmetry with respect to φ in the considered two-dimensional case. The choice of M and R as even integers guarantees a well-defined wind direction, as it is needed below. The definition of $\Delta\epsilon$ allows us to evaluate the collision integral of the POP interaction without a smearing of the Dirac distribution related to the energy conservation. The integer numbers N_v must be chosen in a way so that the maximum energies $\epsilon^v_{\max} = \epsilon^v_{N_v}$ guarantee that $\Phi_v(t,x,y,\epsilon^v_{\max},\mu,\varphi)$ are negligible for all t, x, y, μ, φ and $v = \Gamma, L$.

Next, we approximate the unknown functions Φ_v as the finite sums

$$\Phi_v(t,x,y,\epsilon,\mu,\varphi) \approx \sum_{i=1}^{N_v} \sum_{j=1}^{M} \sum_{k=1}^{R} n^v_{ijk}(t,x,y)\delta(\epsilon - \epsilon^v_i)\delta(\mu - \mu_j)\delta(\varphi - \varphi_k) \tag{14}$$

containing $N_v \times M \times R$ unknown coefficients n^v_{ijk} and the Dirac distributions δ with the poles $\epsilon^v_i = \Delta_{0v} + (i+1/2)\Delta\epsilon$, $i = 1,2,\ldots,N_v$, $\mu_j = (j+1/2)\Delta\mu - 1$, $j = 1,2,\ldots,M$ and $\varphi_k = (k+1/2)\Delta\varphi$, $k = 1,2,\ldots,R$. The ansatz (14) implies that the macroscopic quantity $\langle m(t,x,y)\rangle$ to the microscopic one, $m(\epsilon,\mu,\varphi)$, can be evaluated via

$$\langle m(t,x,y)\rangle = \sum_{v=\Gamma,L} \frac{Z_v}{2\pi^3} \sum_{i=1}^{N_v} \sum_{j=1}^{M} \sum_{k=1}^{R} m(\epsilon^v_i, \mu_j, \varphi_k) n^v_{ijk}(t,x,y), \tag{15}$$

as it can easily be verified by forming moments of (14).

The evolution equations of the coefficients n^v_{ijk} are constructed as suggested by the method of weighted residuals [19]. The ansatz (14) is inserted into the BTE (7) and the result is successively integrated over the cells $\mathscr{D}^v_{ijk} = [\epsilon^v_{i-1/2}, \epsilon^v_{i+1/2}] \times [\mu_{j-1/2}, \mu_{j+1/2}] \times [\varphi_{k-1/2}, \varphi_{k+1/2}]$. In addition, we apply an upwind scheme in the force term together with a linear approximation of the fluxes through the boundaries of the cells controlled by a MinMod slope limiter [20]. This procedure yields a closed set of $N_v \times M \times R$ partial differential equations for each of the valleys $v = \Gamma, L$. It reads

$$\begin{aligned}&\frac{\partial n^v_{ijk}}{\partial t} + \frac{\partial}{\partial x}(g^v_{1,ijk} n^v_{ijk}) + \frac{\partial}{\partial y}(g^v_{2,ijk} n^v_{ijk}) + h^v_{3,i+\frac{1}{2},jk} - h^v_{3,i-\frac{1}{2},jk} + h^v_{4,i,j+\frac{1}{2},k} - h^v_{4,i,j-\frac{1}{2},k} + h^v_{5,ij,k+\frac{1}{2}} - h^v_{5,ij,k-\frac{1}{2}} \\ &\quad = \sum_{a=1}^{N_v} \sum_{b=1}^{M} \sum_{c=1}^{R} \left[\langle S^{\mu v}_{abc,ijk}\rangle n^\mu_{abc} - \langle S^{v\mu}_{ijk,abc}\rangle n^v_{ijk} \right]\end{aligned} \tag{16}$$

with $i = 1,2,\ldots,N_v$, $j = 1,2,\ldots,M$ and $k = 1,2,\ldots,R$. The collision coefficients for the scattering mechanism ξ are evaluated via

$$\langle S^{\xi,v\mu}_{ijk,abc}\rangle = \int_{\mathscr{D}^v_{ijk}} \mathrm{d}\mathbf{S} \int_{\mathscr{D}^\mu_{abc} \cup \tilde{\mathscr{D}}^\mu_{abc}} \mathrm{d}\mathbf{S}' \mathscr{D}_\mu(E') S^\xi_{v\mu}(\mathbf{k}_v, \mathbf{k}'_\mu) \delta(\epsilon - \epsilon^v_i) \delta(\mu - \mu_j) \delta(\varphi - \varphi_k) \tag{17}$$

with $\tilde{\mathscr{D}}^\mu_{abc} = [\epsilon^\mu_{a-\frac{1}{2}}, \epsilon^\mu_{a+\frac{1}{2}}] \times [\mu_{b-\frac{1}{2}}, \mu_{b+\frac{1}{2}}] \times [2\pi - \varphi_{k+\frac{1}{2}}, 2\pi - \varphi_{k-\frac{1}{2}}]$. The numerical fluxes $h^v_{3,i\pm\frac{1}{2},jk}$ are given by

$$h^v_{3,i+\frac{1}{2},jk} = \begin{cases} g^v_{3,i+\frac{1}{2},jk}(n^v_{ijk} + s^v_{ijk}), & g^v_{3,ijk} > 0, \\ g^v_{3,i+\frac{1}{2},jk}(n^v_{i+1,jk} - s^v_{i+1,jk}), & g^v_{3,ijk} < 0, \end{cases} \tag{18a}$$

$$h^v_{3,i-\frac{1}{2},jk} = \begin{cases} g^v_{3,i-\frac{1}{2},jk}(n^v_{ijk} - s^v_{ijk}), & g^v_{3,ijk} < 0, \\ g^v_{3,i-\frac{1}{2},jk}(n^v_{i-1,jk} + s^v_{i-1,jk}), & g^v_{3,ijk} > 0, \end{cases} \tag{18b}$$

$$s^v_{ijk} = \frac{1}{2}\mathrm{MM}(n^v_{i+1,jk} - n^v_{ijk}, n^v_{ijk} - n^v_{i-1,jk}) \tag{18c}$$

with the MinMod scheme

$$\mathrm{MM}(a,b) = \begin{cases} \mathrm{sgn}(a)\min(|a|,|b|), & ab > 0, \\ 0, & \text{otherwise}. \end{cases} \tag{19}$$

Similar expressions are used to determine $h^v_{4,i,j\pm 1/2,k}$ and $h^v_{5,ij,k\pm 1/2}$.

For treating the spatial dependence of the coefficients n^v_{ijk} in the multigroup Eqs. (16), we apply a fifth-order WENO scheme to cope with the strong variations of the electron distributions in space due to, e.g., sharp doping profiles [6,14]. Therefore, we discretize the spatial variables equidistantly

$$x_n = n\Delta x, \quad n = 0,1,\ldots,P, \ \ \Delta x = \frac{L_x}{P}, \tag{20a}$$

$$y_m = m\Delta y, \quad m = 0,1,\ldots,Q, \ \ \Delta y = \frac{L_y}{Q}, \tag{20b}$$

where L_x and L_y are the dimensions of the device. Next, we approximate the spatial derivatives in (16), for instance, that with respect to y, as

$$\frac{\partial}{\partial y}[g^{v}_{2,ijk} n^{v}_{ijk}(t, x_n, y_m)] \approx \frac{1}{\Delta y}\left(\hat{h}_{m+\frac{1}{2}} - \hat{h}_{m-\frac{1}{2}}\right) \tag{21}$$

for fixed indices i, j, k, n and fixed time t. Therefore, these parameters are not written down in the numerical fluxes $\hat{h}_{m\pm1/2}$ to keep the description concise. We note that the wind direction, i.e., the sign of $g^{v}_{2,ijk}$ is well-defined because of the chosen discretization (13a), and it is independent of m. Thus, for fixed i, j, k, the wind direction is fixed. Moreover, the coefficients $n^{v}_{ijk}(t, x_n, y_m)$ are positive for physically relevant initial conditions so that flux splitting is not necessary. We define

$$h_m = g^{v}_{2,ijk} n^{v}_{ijk}(t, x_n, y_m), \quad m = -3, -2, \ldots, Q+3 \tag{22}$$

for fixed i, j, k, n and use them to determine the numerical fluxes $\hat{h}_{m+\frac{1}{2}}$ by means of the fifth-order WENO scheme proposed in [14]. In (22), fluxes are defined in points, the so-called ghost points, which do not belong to the considered device. They must be chosen to suitably model the demanded boundary conditions. For instance, we consider a boundary at $y = y_Q$. For simulating reflecting boundaries, we set

$$n^{v}_{ijk}(t, x_n, y_{Q+m}) = n^{v}_{ijk}(t, x_n, y_{Q+1-m}), \quad m = 1, 2, 3, \tag{23a}$$

according to [6], which implies that $\hat{h}_{Q+1/2} = 0$. The Schottky contacts are modeled as totally absorbing contacts. Hence, we apply

$$n^{v}_{ijk}(t, x_n, y_{Q+m}) = \begin{cases} n^{v}_{ijk}(t, x_n, y_Q), & g^{v}_{ijk} > 0, \\ 0, & g^{v}_{ijk} < 0, \end{cases} \quad m = 1, 2, 3 \tag{23b}$$

for determining the fluxes in the ghost-points at such contacts. Finally, the ohmic contacts are simulated via

$$n^{v}_{ijk}(t, x_n, y_{Q+m}) = \begin{cases} n^{v}_{ijk}(t, x_n, y_Q), & g^{v}_{ijk} > 0, \\ n^{M,v}_{ijk}(x_n, y_Q), & g^{v}_{ijk} < 0, \end{cases} \quad m = 1, 2, 3. \tag{23c}$$

Here, the coefficient $n^{M,v}_{ijk}$ are obtained from Maxwell distributions, which are normalized to the donor density

$$n^{M,v}_{ijk}(x_n, y_m) = N_{\mathrm{D}}(x_n, y_m)\frac{\int_{D^{v}_{ijk}} \mathrm{d}\mathbf{S}\mathscr{D}_v(\epsilon)\exp\left(-\frac{\epsilon}{k_{\mathrm{B}}T_{\mathrm{L}}}\right)}{\sum_{\mu=\Gamma,L}\frac{Z_\mu}{4\pi^3}\int_D \mathrm{d}\mathbf{S}\mathscr{D}_\mu(\epsilon)\exp\left(-\frac{\epsilon}{k_{\mathrm{B}}T_{\mathrm{L}}}\right)}. \tag{24}$$

In addition, we set $\hat{h}_{Q+1/2} = C(t, x_n) g^{v}_{ijk} n^{M,v}_{ijk}(x_n, y_Q)$ for $g^{v}_{ijk} < 0$, where the factor $C(t, x_n)$ is determined so that the charge neutrality at the contact is fulfilled.

The combination of the multigroup equations (16) with the WENO scheme (21) leads to a set of $N_v \times M \times R \times P \times Q$ ordinary differential equations in time for each of the considered valleys v. The time integration is performed by means of the TVD forward Euler scheme [21], where the time step Δt is chosen so that the CFL condition for guaranteeing stability of the numerical procedure is fulfilled. Thus, we determine the time step via

$$\Delta t = \frac{C_{\mathrm{CFL}}}{\max\left(\frac{|g^{v}_1|}{\Delta x} + \frac{|g^{v}_2|}{\Delta y} + \frac{|g^{v}_3|}{\Delta \epsilon} + \frac{|g^{v}_4|}{\Delta \mu} + \frac{|g^{v}_5|}{\Delta \varphi}\right)} \tag{25}$$

with $C_{\mathrm{CFL}} = 0.8$ and update it in the simulation for taking into account the changing of the electric fields (cp. (11a)). The Poisson equation (12b) is solved with the help of a standard Successive Over-Relaxation (SOR) scheme [1] at each time step with the modified charge density obtained from the multigroup-WENO

equations. At the initial time t_0, we set the electron distribution functions to the equilibrium Maxwellians (24), i.e., $n_{ijk}^{v}(t_0, x_n, y_m) = n_{ijk}^{M,v}(x_n, y_m)$.

We close this section with some remarks on the numerical procedures used for approximating the terms of the BTEs. From a mathematical point of view, the multigroup approach for treating the collision terms of the BTEs corresponds to the midpoint rule. Therefore, this approximation is of second-order and it is consistent to apply the second-order MinMod scheme for handling the force term. In [5–8], the collision terms of the BTEs are evaluated with the help of a similar procedure as we do, so that the use of a fifth-order WENO technique for treating the force terms does not increase the accuracy of the method. Moreover, the choice of values for ghost points in the momentum space as it is necessary when using the WENO code, is a tricky problem, while our approach is rid of such difficulties. Finally, the collision terms smooth out the electron distribution functions in the wave vector space, which prevents the electric field from forming sharp gradients in Φ_v as functions of energy and angles. That is why we think that our multigroup approach for handling the dependence of the distribution function on the wave vector is certainly an appropriate choice. On the other hand, the application of the high-order WENO scheme in physical space is absolutely necessary for stopping the sharp gradients in the doping concentration from acting as the origins of spurious oscillations. Apart from these regions of the device, the electron distribution function is also very smooth in the real space, and the WENO technique can bring to bear its high efficiency for hyperbolic systems. At the first glaze, it might be surprising why we combine the second-order multigroup and the fifth-order WENO procedure with the Euler rule for performing the time integration, which is only of first order. This choice is motivated on physical grounds. The temporal evolution from the unphysical initial conditions mentioned above towards the stationary state is not of practical interest. Hence, this relaxation can be treated by the not very accurate, but fast and simple Euler scheme. However, we get accurate results for the stationary state, since the steady-state distribution does not depend on the way as it is reached. For the investigation of a real time dependent problem, for instance, a switching process, the so obtained stationary-state results can be used as initial data. The further temporal evolution can then be studied with the help of a scheme that is consistent with the rest of the numerical procedure, for example, the second-order TVD Runge–Kutta method proposed in [21].

4. Numerical results

In this section, we present the results for the electron transport through a GaAs-MESFET obtained by means of our multigroup-WENO solver (16), (21). All of the calculations are performed at the lattice temperature $T_{\mathrm{L}} = 300$ K. The material parameters used are given in Table 2. These values are the same

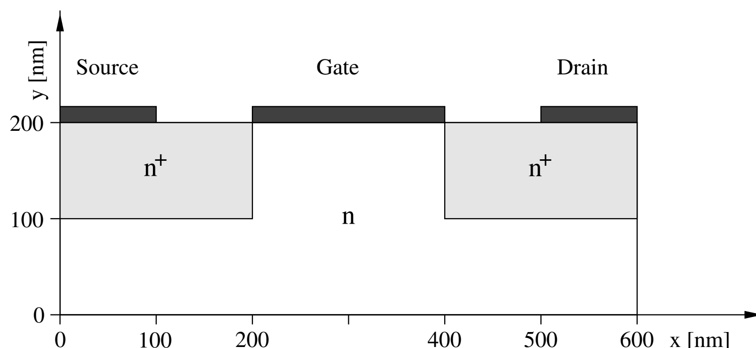

Fig. 1. Schematic illustration of the considered MESFET geometry.

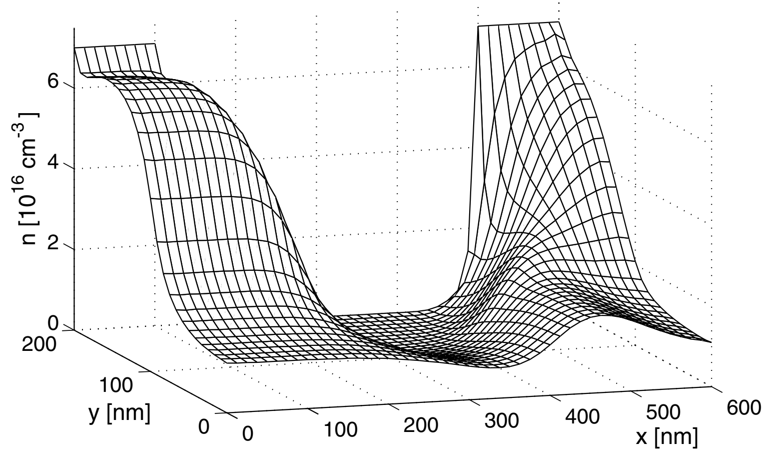

Fig. 2. Electron density n versus position (x,y) in the GaAs-MESFET at $t = 4$ ps.

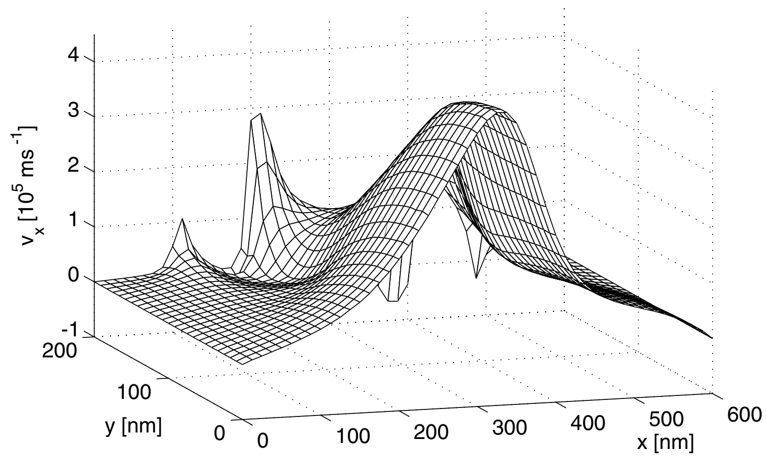

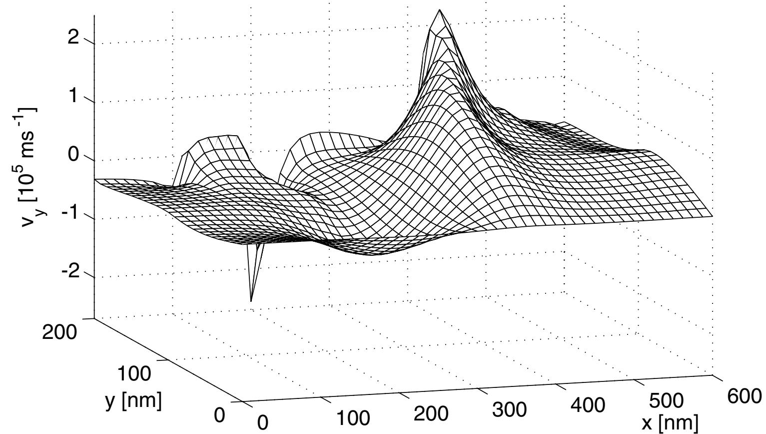

Fig. 3. X-component v_x and y-component v_y of the drift velocity versus position (x, y) at $t = 4$ ps.

as given in [8] and they equal approximately the data proposed in [16,17]. The geometry of the investigated GaAs-MESFET is shown in Fig. 1. The donor densities are chosen as $n^+ = 7 \times 10^{16}$ cm^{-3} and $n = 10^{16}$ cm^{-3}. The source and drain contacts act as particle reservoirs. Electrons may enter or exit through these contacts, which is modelled according to (23c). The Schottky contact at the gate is assumed to be a totally absorbing boundary (23b), whereas perfectly reflecting boundary conditions are imposed at the non-contact surfaces (23a). Concerning the boundary conditions for the Poisson equation, we apply the Neumann condition (vanishing electric field in the direction normal to the surface) on the non-contact boundaries to simulate insulating boundaries. The source, gate and drain contacts are treated as Dirichlet boundaries, where the bias voltages of $V_S = 0$ V at the source, $V_G = -0.4$ V at the gate and $V_D = 0.8$ V at the drain are applied. All of these boundary conditions are chosen as it is the standard for basic MESFET simulations. However, we remark that for the investigations of real devices, these settings must certainly be questioned.

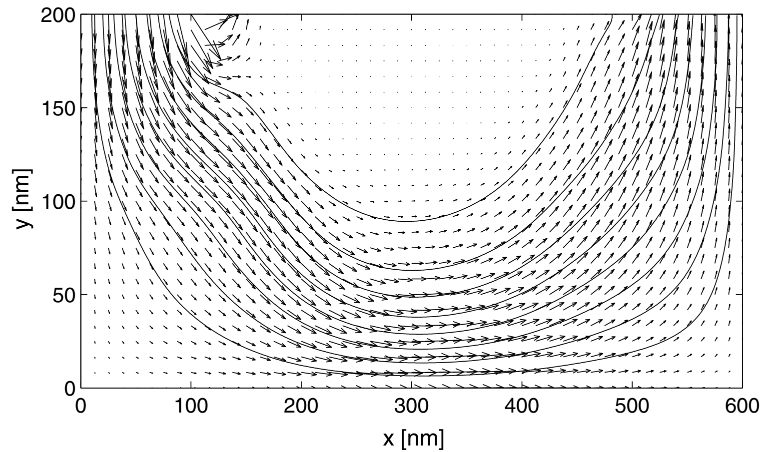

Fig. 4. Velocity field and current lines at $t = 4$ ps.

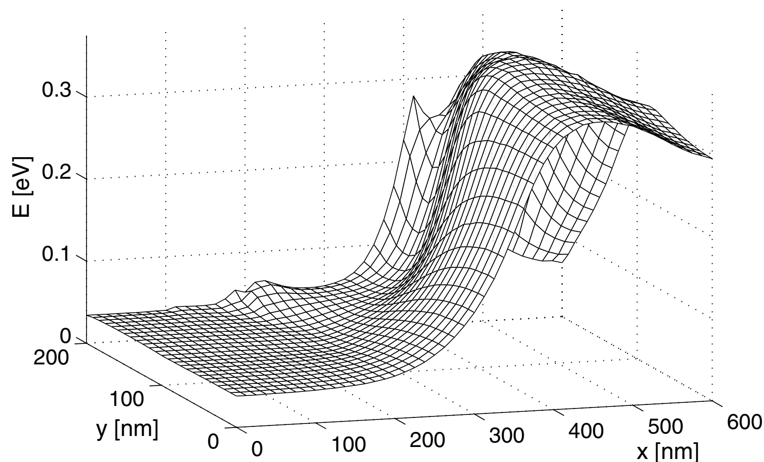

Fig. 5. Mean electron energy E versus position (x, y) at $t = 4$ ps.

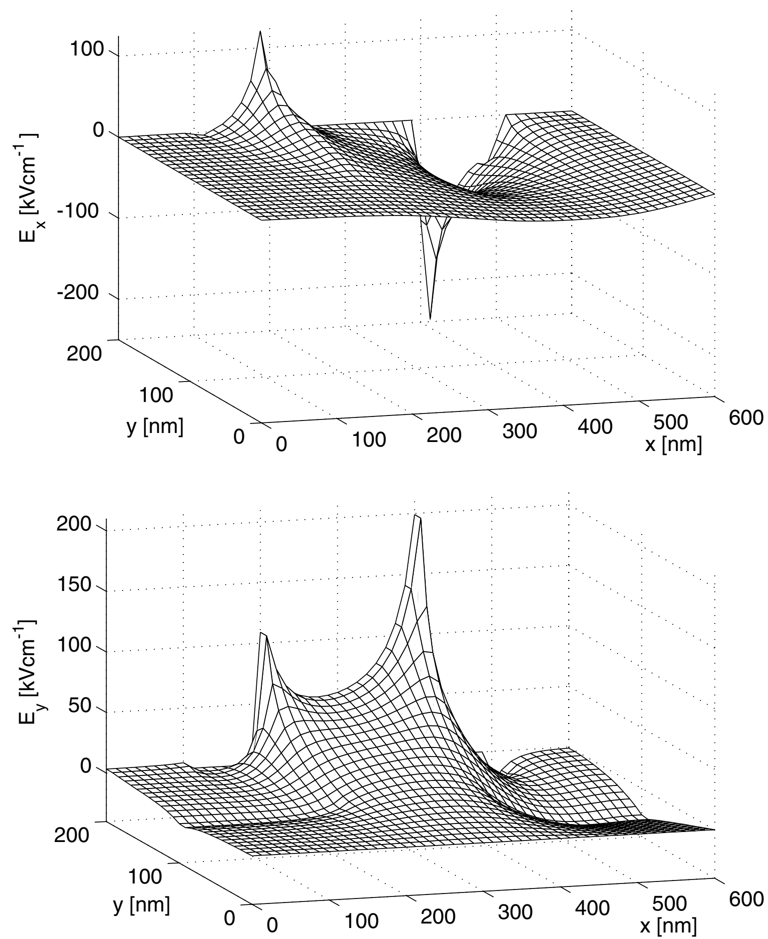

Fig. 6. X-component E_x and y-component E_y of the electric field versus position (x, y) at $t = 4$ ps.

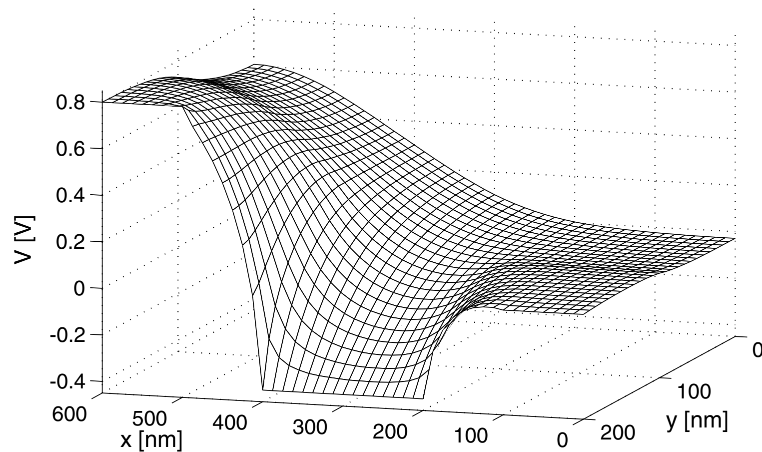

Fig. 7. Electrostatic potential V versus position (x, y) at $t = 4$ ps.

The parameters of the grid are chosen as $N^{\Gamma} = 50$, $N^{\mathrm{L}} = 30$, $n_{\mathrm{mul}} = 2$, $M = R = 10$ for the momentum space together with $P = 48$, $Q = 24$ grid points in real space. The time integration is performed from the initial time $t_0 = 0$ ps up to the final time $t = 4$ ps, when the stationary state is approximately reached.

In Figs. 2–5, the most important hydrodynamic transport quantities, namely the electron density, the components of the drift velocity, the velocity field and the mean electron energy are displayed. First of all, we point out the highly regular, non-oscillatory behavior of these quantities throughout the whole device. This behavior implies that the proposed numerical technique is able to resolve the spatial dependence of transport quantities even in regions of very low electron densities and at abrupt changes of the donor density.

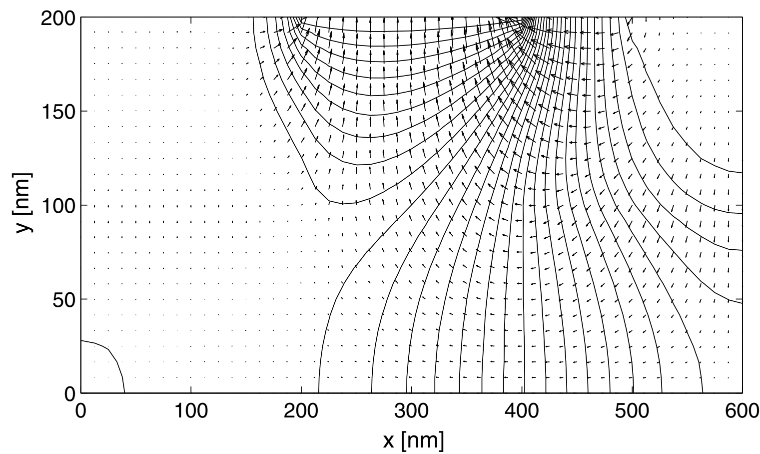

Fig. 8. Electric field and equipotential lines at $t = 4$ ps.

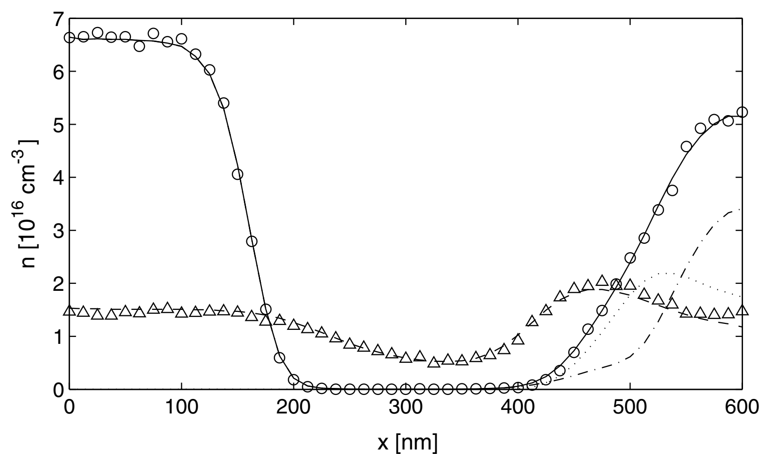

Fig. 9. Electron density n versus position x in the GaAs-MESFET at $t = 4$ ps. The lines refer to present results, the symbols depict Monte Carlo data. (– – –, △) electron density at $y = 50$ nm; (————-, ○) electron density at $y = 150$ nm; (– · –) Γ-electron density at $y = 150$ nm; (· · ·) L-electron density at $y = 150$ nm.

Concerning the electron density in Fig. 2, we observe the formation of a depletion layer at the gate contact, since strong electric fields repulse the carriers from this region. In this respect, the behavior of the GaAs-MESFET agrees with that of the silicon MESFET, studied in detail in [7,10]. On the other hand, the charge accumulation, which is formed around the drain n–n^+ interface, is not found in the corresponding silicon device. As discussed in [9,17] for the GaAs n^+–n–n^+ diode, this enhanced electron density near the drain results from the backscattering of carriers into the active region after having already entered the high doping drain region. Due to this typical multi-valley effect, the anode contact cannot be simply treated as a drain for the electrons in the designing of submicron GaAs devices, since this region has a strong influence on the distribution of electrons in the active zone. In addition, we observe a sharp drop of the electron density at the source contact, which does not seem reasonable at the first glance. However, since we also found this drop in the corresponding MC calculation, this behavior must be a consequence of the used boundary condition and not an artefact of our numerical scheme.

In the x- and the y-component of the electron drift velocity in Fig. 3, we find values which exceed the maximum drift velocity of bulk GaAs (about 1.8×10^5 m s^{-1} at room temperature [9]) significantly. Thus, ballistic transport plays an important role in the considered device. A more descriptive illustration of the

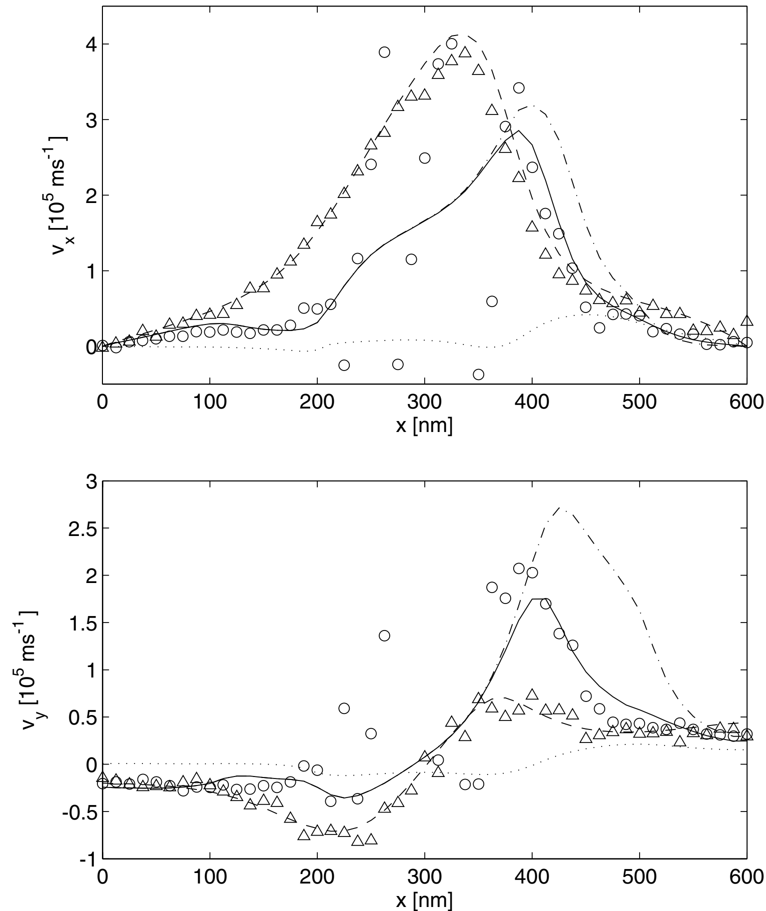

Fig. 10. X-component v_x and y-component v_y of the drift velocity versus position x at $t = 4$ ps. The lines refer to present results, the symbols depict Monte Carlo data. (– – –, △) drift velocity at $y = 50$ nm; (———-, ○) drift velocity at $y = 150$ nm; (– · –) Γ-drift velocity at $y = 150$ nm; (· · ·) L-drift velocity at $y = 150$ nm.

electron drift velocity is given in Fig. 5. Here, we display the electron velocity field and some current lines. Although this representation gives only qualitative information, it offers a simple way for studying the transport of the electrons through the device.

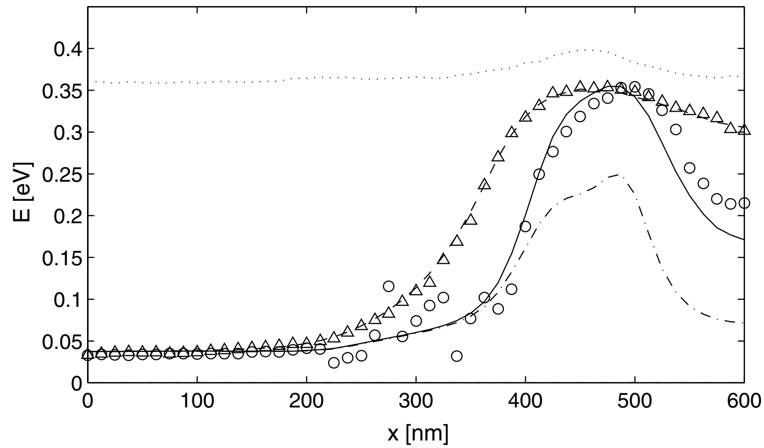

Fig. 11. Mean electron energy E versus position x at $t = 4$ ps. The lines refer to present results, the symbols depict Monte Carlo data. (−−−, △) electron energy at $y = 50$ nm; (———, ○) electron energy at $y = 150$ nm; (− · −) Γ-electron energy at $y = 150$ nm; (···) L-electron energy at $y = 150$ nm.

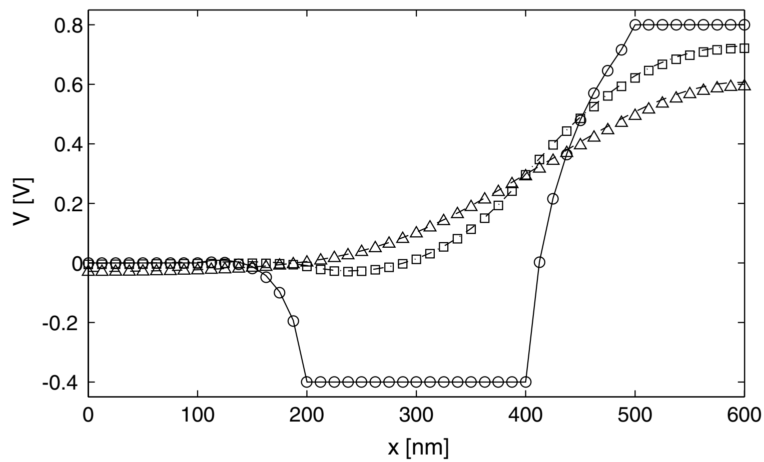

Fig. 12. Electrostatic potential V versus position x at $t = 4$ ps. The lines refer to present results, the symbols depict Monte Carlo data. (−−−, △) potential at $y = 0$ nm; (− · −, □) potential at $y = 100$ nm; (———, ○) potential at $y = 200$ nm.

Table 3
Number of grid points used in the simulations A, B and C

Simulation	n_{mul}	N^{Γ}	N^{L}	M	R	P	Q	Total
A	2	50	30	10	10	48	24	9,216,000
B	1	25	15	8	6	30	16	921,600
C	1	25	15	4	4	18	8	92,160

The mean electron energy in Fig. 4 equals approximately the mean lattice energy $3k_BT_L/2$ in the source region. In the active region, the electrons are accelerated by strong electric fields and gain energy, leading to a maximum electron energy at the drain n–n^+ interface. At the drain contact, the mean energy is low again. This is caused by the fact that the electrons lose their energies in several scattering events and that hot, i.e., high energetic outflowing electrons are replaced by cold inflowing carriers.

For illustrating the electrical properties of the considered GaAs-MESFET, we display the x- and the y-components of the electric field as well as the electrostatic potential versus position in Figs. 6 and 7. The potential is very regular, while the components of the electric fields feature some spikes due to their singularities in the points of changing boundary conditions. Additionally, we find strong y-components of the field repulsing the electrons from the gate, as well as the back-drawing fields at the changes in the doping concentration. An illustrative summary of Figs. 6 and 7 is given in Fig. 8 depicting the electric field and the equipotential lines in the MESFET at $t = 4$ ps.

For the validation of our numerical scheme, we compare our results with those of Monte Carlo calculations, which are obtained by the code of Tomizawa [17]. This code has been slightly modified concerning the scattering rates used, which allows us a suitable comparison of the deterministic and the stochastic results. We show some cuts of the electron density, the drift velocity, the mean energy and the electrostatic potential in Figs. 9–12. We find that all of the displayed cuts of the electrostatic potential as well as all of the hydrodynamic quantities at $y = 50$ nm agree very well. In addition, the cuts at $y = 150$ nm exhibit the same good consistency in the regions where the electron density is not too small. We also observe that the Monte Carlo method is not able to determine the macroscopic quantities in the depletion layer in a sufficiently accurate order, while our deterministic technique allows us the investigation of this region.

Besides the total electron density, velocity and energy, we also display the portions of these quantities due to Γ- and L-electrons for $y = 150$ nm. We find that the transport is dominated by Γ-electrons between $x = 0$ and $x = 300$ nm. For x-values higher than 300 nm, electrons have gained high enough energies so that a significant portion of them is scattered into the L-valleys and the total macroscopic quantities set up by a complicated interplay of Γ- and L-electrons. We observe that there are more L-electrons than Γ-electrons between $x = 400$ and $x = 550$ nm. The L-drift velocity is low in comparison to the Γ-velocity as a consequence of the high effective mass of L-electrons and the very efficient equivalent intervalley scattering in these valleys. Finally, we find that both the Γ- and the L-electrons are significantly heated in the drain region.

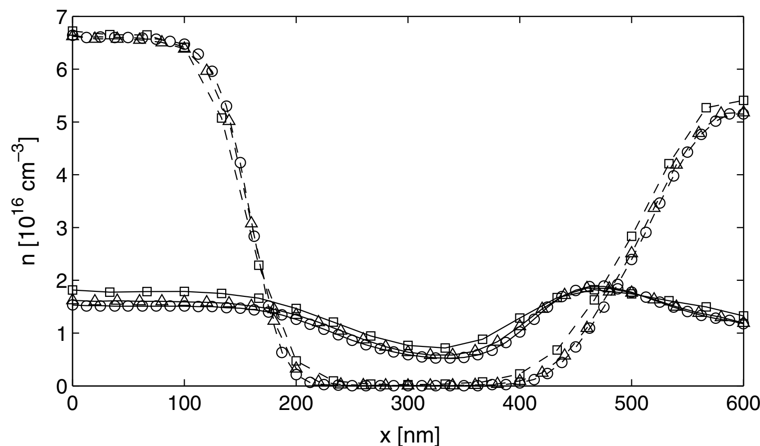

Fig. 13. Electron density n versus position x in the GaAs-MESFET at $t = 4$ ps. The solid lines refer to $y = 50$ nm, the dashed lines refer to $y = 150$ nm. (○) simulation A; (△) simulation B; (□) simulation C.

For studying the influence of the number of grid points on the obtained results, the electron transport in the GaAs-MESFET was not only simulated with the help of the fine grid mentioned above (simulation A), but also with a medium (simulation B) and a coarse grid (simulation C). Details on these discretizations are given in Table 3. We note that the total number of unknowns behaves like A:B:$C = 100$:10:1.

Figs. 13–15 illustrate cuts of the electron density, the x- and the y-component of the drift velocity as well as the mean electron energy at $t = 4$ ps, for $y = 50$ and $y = 150$ nm. For the electron density, we find that the results of the three simulations agree well; especially the differences in the data of the simulations A and B are very small. Concerning the drift velocity and the mean energy, the same statement is true for $y = 50$ nm. Here, only the maximum values of the drift velocity differ notably in the simulations A, B and C. At $y = 150$ nm, these quantities only exhibit good agreement outside the depletion layer, while for an accurate investigation of the depletion layer a fine grid is necessary. However, the results of the simulations B and C are still more meaningful than the corresponding data of the MC calculation.

In Fig. 16, we display the temporal evolution of the boundary y_D of the depletion layer, which we implicitly define as $n[t,x,y_D(t,x)] = 0.75 \times 10^{22}$ m^{-3}. Of course, the studied evolution process is not physically

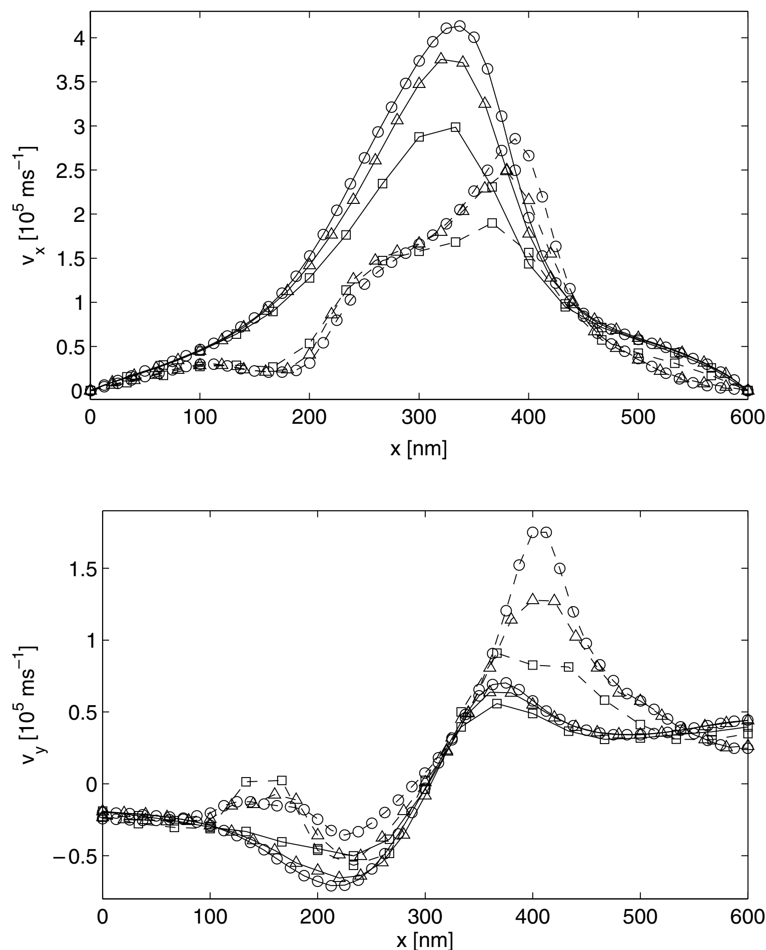

Fig. 14. X-component v_x and y-component v_y of the drift velocity versus position x in the GaAs-MESFET at $t = 4$ ps. The solid lines refer to $y = 50$ nm, the dashed lines refer to $y = 150$ nm. (○) simulation A; (△) simulation B; (□) simulation C.

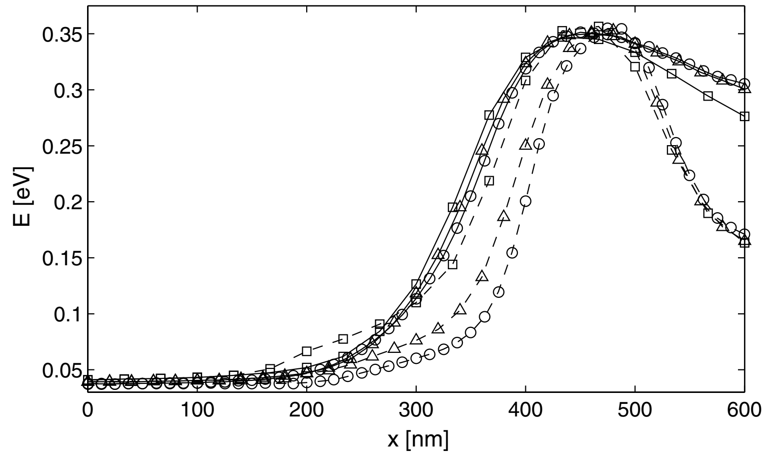

Fig. 15. Mean electron energy E versus position x in the GaAs-MESFET at $t = 4$ ps. The solid lines refer to $y = 50$ nm, the dashed lines refer to $y = 150$ nm. (○) simulation A; (△) simulation B; (□) simulation C.

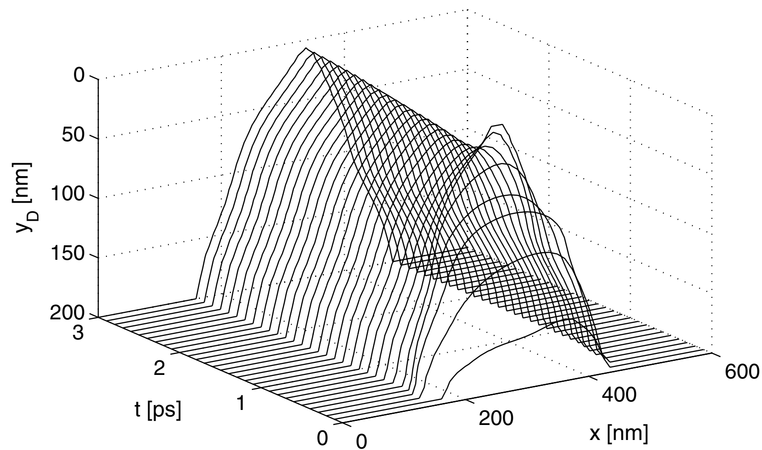

Fig. 16. Temporal evolution of the boundary of the depletion layer $y_D(t, x)$.

relevant, since the initial conditions are not. However, Fig. 16 allows us to cherish hopes for the applicability of our numerical scheme to investigate time dependent problems, and it shows some interesting features of the depletion layer, which should also influence the behavior of real MESFETs in switching processes. We observe that the depletion layer is not formed by a simple evacuation of electrons, but its formation exhibits a temporal periodic structure. Rapid increasing of the depletion layer at $t = 0.3$ and $t = 0.6$ ps is followed by a much smaller growth or even a reduction of the y_D. Similarly, an oscillation between more and less symmetric depletion layers is visible. After $t = 1$ ps, the depletion layer evolves quite slowly to its stationary state shape, which is almost reached at $t = 3$ ps.

One of the advantages of deterministic methods for solving the Boltzmann transport equation is the availability of the electron distribution function for all times and positions in noise-free resolution. For instance, we depict the distribution functions for electrons in the Γ- and in the L-valley versus energy and polar angle at the point $x = 500$ nm, $y = 150$ nm at $t = 4$ ps in Fig. 17. It should be noted that these functions are obtained by averaging the coefficients n^{v}_{ijk} with respect to the azimuth angle φ, which allows

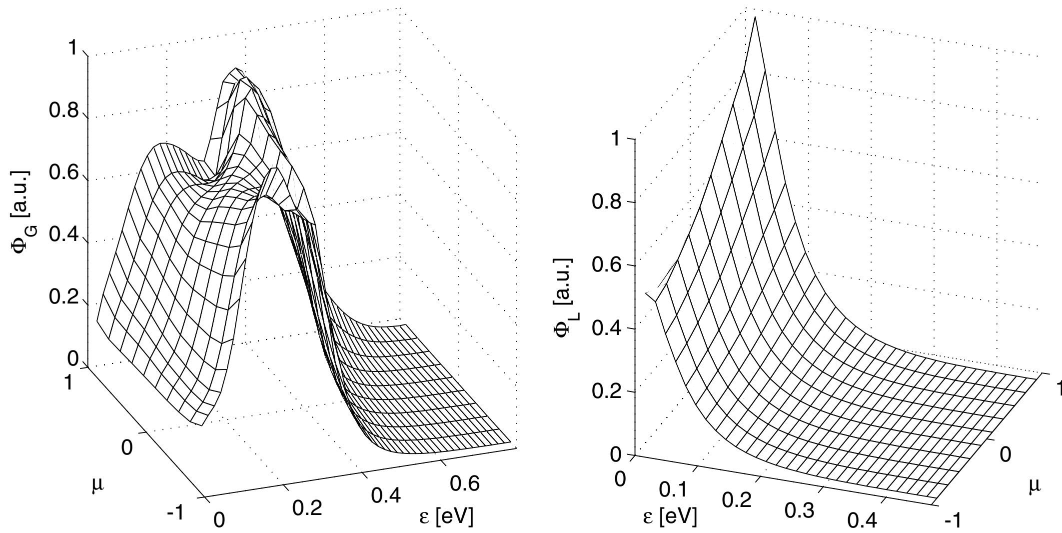

Fig. 17. Normalized electron distribution Φ_G in the Γ-valley and Φ_L in the L-valley at $t = 4$ ps in the point $x = 500$ nm, $y = 150$ nm.

the convenient representation. We find that both, the Γ- and the L-distribution function, are very smooth. The distribution of L-electrons can be seen as a shifted Maxwell distribution with a temperature much higher than the lattice temperature. On the other hand the, Γ-distribution function is assigned to a complicated structure, and it is far from equilibrium. Consequently, the application of hydrodynamic transport equations for the investigation of the presented submicron GaAs-MESFET cannot yield accurate results.

Finally, we report the results for the drain characteristics of the considered GaAs-MESFET in Fig. 18 in comparison to the results of Monte Carlo simulations. The drain current I_D is obtained from the momentum nv_y at the drain via

$$I_D(t) = -\mathcal{Q} \sum_{x_n \in \mathrm{drain}} nv_y(t, x_n, y_Q)\Delta x. \tag{26}$$

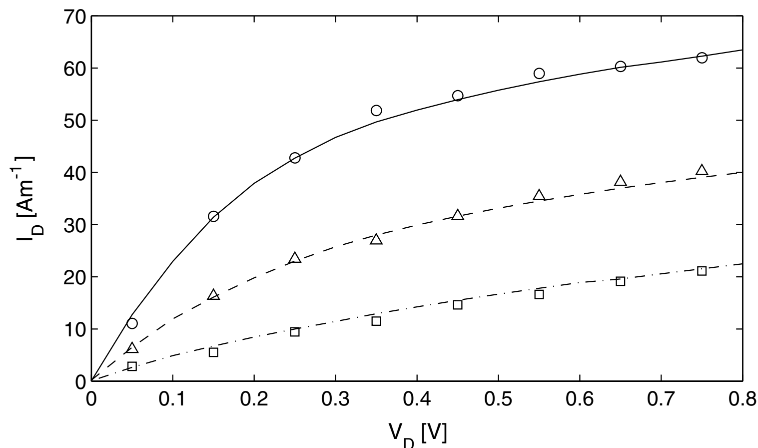

Fig. 18. Steady state drain current I_D versus drain voltage V_D for several gate voltages. Lines refer to present results, symbols denote Monte Carlo data. (———, ○) $V_G = -0.2$ V, (– – –, △) $V_G = -0.4$ V, (– · –, □) $V_G = -0.6$ V.

The stationary state is assumed to be reached, when the relative change of I_D and the source current I_S is less than 1% within a time interval of 0.2 ps. All of the calculations for determining the drain characteristics are performed with the grid $N^\Gamma = 25$, $N^L = 15$, $n_{mul} = 1$, $M = R = 4$ in momentum space and $P = 18$, $Q = 10$ in real space. Concerning the shape of the drain characteristics, we find the typical behavior of a MESFET [17,22]. Moreover, we observe a very good agreement of the deterministic and the stochastic results. This implies that the presented numerical technique is able to give sufficiently accurate information on the main transport features of a device even when a very coarse grid is used.

5. Conclusion

We present a direct multigroup-WENO solver for the Boltzmann–Poisson system describing the electron transport in spatially two-dimensional semiconductor devices. The model equations are constructed in a way that they allow the investigation of devices based on GaAs, which is featured by a complicated band structure and by the fact that some of the main scattering mechanisms, i.e., the polar optical scattering and the impurity scattering, are anisotropic.

Several numerical results on the main transport quantities in a GaAs-MESFET as well as their comparison to the data of Monte Carlo simulations prove the applicability and the validity of the proposed numerical scheme. The presented method is not competitive with Monte Carlo simulations on the level of computational costs for determining stationary states with the fine grid (about two days on two AMD Athlon MP 2000+ processors, 1666 MHz, 2 GB RAM). However, it provides detailed, highly accurate information on distribution functions and on macroscopic quantities in the whole device. Therefore, the multigroup-WENO solver can usefully be applied for creating benchmarks for all of the solvers for semiconductor device simulation. On the other hand, the presented numerical scheme gives sufficiently accurate results even for coarse grids, which allows the obtaining of a noise-free overview of the main transport properties of a device within justifiable computation times (about 20 min for determining the 17 points of one of the current-voltage curves in Fig. 18 with one of the mentioned processors).

Hence, the multigroup-WENO solver is found to be a powerful tool for GaAs device simulation and an interesting alternative to the usually applied Monte Carlo techniques.

Acknowledgement

This work has been supported by the Fond zur Förderung der wissenschaftlichen Forschung, Vienna, under Contract No. P17438-N08.

References

[1] C. Jacoboni, P. Lugli, The Monte Carlo Method for Semiconductor Device Simulation, Springer, Vienna, 1989.
[2] B. Niclot, P. Degond, F. Poupaud, Deterministic simulations of the Boltzmann transport equations of semiconductors, J. Comput. Phys. 78 (1988) 313–349.
[3] E. Fatemi, E. Odeh, Upwind finite difference solution of Boltzmann equations applied to electron transport in semiconductor devices, J. Comput. Phys. 108 (1993) 209–217.
[4] A. Majorana, R.M. Pidatella, A finite difference scheme solving the Boltzmann–Poisson system for semiconductor devices, J. Comput. Phys. 174 (2001) 349–668.
[5] J.A. Carrillo, I.M. Gamba, A. Majorana, C.-W. Shu, A WENO solver for the 1D non-stationary Boltzmann–Poisson systems for semiconductor devices, J. Comput. Electron. 1 (2002) 365–376.
[6] J.A. Carrillo, I.M. Gamba, A. Majorana, C.-W. Shu, A WENO solver for the transients of Boltzmann–Poisson system for semiconductor devices: performance and comparison with Monte Carlo methods, J. Comput. Phys. 184 (2003) 498–525.

[7] J.A. Carrillo, I.M. Gamba, A. Majorana, C.-W. Shu, A direct solver for 2D non-stationary Boltzmann–Poisson systems for semiconductor devices: a MESFET simulation by WENO-Boltzmann schemes, J. Comput. Electron. 2 (2003) 375–380.
[8] M.J. Cáceres, J.A. Carrillo, A. Majorana, Deterministic solution of the Boltzmann–Poisson system in GaAs-based semiconductors, SIAM J. Scient. Comp. (to appear) HYKE preprint HYKE2004-111, www.hyke.org (2004).
[9] M. Galler, F. Schürrer, A deterministic solver for the 1D non-stationary Boltzmann–Poisson system for GaAs devices: bulk GaAs and GaAs n^{+}–n_{i}–n^{+} diode, J. Comput. Electronics (in press).
[10] M. Galler, A. Majorana, F. Schürrer, A multigroup WENO solver for the non-stationary Boltzmann–Poisson system for semiconductor devices, in: Proceedings of 5th International Workshop on Scientific Computing in Electrical Engineering (in press).
[11] M. Galler, F. Schürrer, A deterministic solution method for the coupled system of transport equations for the electrons and phonons in polar semiconductors, J. Phys. A: Math. Gen. 37 (2004) 1479–1497.
[12] M. Galler, F. Schürrer, A multigroup approach to the coupled electron-phonon Boltzmann equations in InP, Trans. Theor. Stat. Phys. 33 (2004) 485–501.
[13] M. Galler, F. Schürrer, Multigroup equations to the hot-electron hot-phonon system in III–V compound semiconductors, Comp. Methods Appl. Mech. Eng. 194 (2005) 2806–2818.
[14] G. Jiang, C.-W. Shu, Efficient implementation of weighted ENO schemes, J. Comput. Phys. 126 (1996) 202–228.
[15] B. Nag, Electron Transport In Compound Semiconductors, Springer, New York, 1980.
[16] M. Lundstrom, Fundamentals of Carrier Transport, Cambridge University Press, Cambridge, 2000.
[17] K. Tomizawa, Numerical Simulation of Submicron Semiconductor Devices, Artech House, Boston, 1993.
[18] J.M. Ziman, Electrons and Phonons, Clarendon Press, Oxford, 2001.
[19] L. Lapidus, G.F. Pinder, Numerical Solutions of Partial Differential Equations in Science and Engineering, Wiley, New York, 1982.
[20] R.J. LeVeque, Numerical Methods for Conservation Laws, Birkhäuser, Basel, 1992.
[21] C.-W. Shu, S. Osher, Efficient implementation of essentially non-oscillatory shock capturing schemes, J. Comput. Phys. 77 (1988) 439–471.
[22] S.M. Sze, High-speed Semiconductor Devices, Wiley, New York, 1990.